CO_2 EFFECT ON THE FATIGUE CRACK GROWTH OF X80 PIPELINE STEEL IN HYDROGEN-ENRICHED NATURAL GAS: EXPERIMENT VS DENSITY FUNCTIONAL THEORY CALCULATION

Juan, S.[1,2], Baihui, X.[1], Haotian, W.[1], Zhengli, H.[1,3] and Jinyang, Z.[1,3]

[1] Institute of Process Equipment, Zhejiang University, Hangzhou, 310027, PR China

[2] Graduate School of Engineering, Kyushu University, Fukuoka, 819-0935, Japan

[3] Zhejiang University Institute of Hydrogen Energy, Hangzhou, 310027, PR China

ABSTRACT

The influence of hydrogen-enriched natural gas (HENG) and CO_2 on the mechanical property of X80 pipeline steel were investigated via fatigue crack growth rate (FCGR) tests and density functional theory (DFT) calculations. The results show that the FCGR in H_2 was slightly faster than that in HENG, while it was slower than that in the $N_2/CO_2/H_2$ mixtures. The enhanced FCGR by CO_2 further increased with the increasing CO_2 content. DFT calculation results show that the adsorbed CO_2 on the iron surface significantly increased the migration rate of H atoms from surface to subsurface. This promotes the entry of hydrogen into the steel.

1.0 INTRODUCTION

Hydrogen is beginning to play a greater role in the transition to clean, safe and sustainable energy systems [1]. Blending hydrogen gas into the natural gas grid is an efficient and economical way of transporting hydrogen on a large scale [2, 3]. Up to now, Germany, France, the UK and some other countries have blended hydrogen gas into the local natural gas grid in the selected area [4-6]. More and more countries plan to launch demonstration projects and try to transport hydrogen-enriched natural gas (HENG) by the national natural gas grid. However, hydrogen atoms are easy to enter into metals, resulting in a large internal hydrogen concentration in the material [7]. Under the right conditions, hydrogen can degrade the mechanical properties of pipeline steels, which is known as hydrogen embrittlement (HE) [7, 8]. HE can be a very complicated process and is a potential threat to the safety of HENG pipelines.

The hydrogen degradation of pipeline steels exposed to a hydrogen-containing environment must be considered in determining the life expectancy of a HENG pipeline delivery system. Many researchers are devoted to studying the HE behaviour of pipeline steel, e.g. X80 and ASTM 1020 steel, in the hydrogen-containing environment [9, 10]. Due to the cost and difficulty of the experiment, most of the tests were conducted in the simulated HENG (N_2/H_2 mixture or CH_4/H_2 mixture) [11, 12]. Methane, which is the major component of natural gas, was proven to have no effect on the mechanical properties of steels [13]. However, there are many other compositions in natural gas, such as O_2, CO, H_2O, H_2S, CO_2 and so on. Some of them, like CO and O_2, act as an inhibitor of the hydrogen-induced fracture of steels [14-17]. However, H_2S and H_2O are reported to enhance the HE of steels [15, 18]. In this case, whether the data obtained in the non-actual HENG can be used as a substitute for the actual HENG to evaluate the life expectancy of the HENG pipeline is a question worth considering.

In our previous studies, fatigue crack growth rate (FCGR) experiments were conducted on GB20# steel in actual HENG and high purity hydrogen gas. It was found that FCGRs have a significant acceleration in actual HENG compared with that in hydrogen gas [19]. CO_2 was found to have an enhancing effect on the HE of this steel. Consistent with the fatigue performance, HENG enhanced the degradation of fracture toughness of this steel as well [20]. C.S. Zhou et al. [13] also investigated the FCGRs of pure iron in actual HENG as well as hydrogen gas and the same tendency was obtained. In addition, hydrogen permeation tests showed that both CO_2 and natural gas could accelerate the diffusion of hydrogen in pure iron [13]. However, for natural gas transportation, many countries built transmission pipelines utilizing higher strength steels of API grade X70 and X80 [18]. The susceptibility to HE of those typical pipeline steels in actual HENG is still unclear.

Regarding the CO_2 effect on the HE of steels in a hydrogen environment, several literatures reported

this phenomenon. H.G. Nelson [21] found that the susceptibility of 1020 steel, which is similar to GB20# steel, to HE in the mixture of CO_2 and H_2 was higher than that in hydrogen gas. M.X. Xiong et al. [18] reported that CO_2 resulted in a significant deterioration of the tensile properties of X80 in an aqueous environment. J.D. Frandsen and H.L. Marcus [14] showed that CO_2 had a small effect on the crack propagation of HP-9-4-20, HY-180 and ASTM A514B steel when it was added to hydrogen. Furthermore, the degree of CO_2 effect on the HE of these three high strength steels varied between steel grades and at different stress intensity factor levels. Additionally, 2.25Cr-1Mo steel was not sensitive to the CO_2 effect in the hydrogen/carbon dioxide mixture, which was shown by the fact that the FCGR in the mixture only increased by 0.01% compared with that in pure hydrogen [22]. To date, the research on the CO_2 effect is less. From the limited previous studies, we are unable to completely clarify the effect of CO_2 on the HE behaviour of different materials. Furthermore, the mechanism of the CO_2 effect still needs further investigation.

In this study, fatigue crack growth rate (FCGR) experiments were carried out on X80 pipeline steel in the actual NG/H_2 mixture, N_2/H_2 mixture, CO_2/H_2/N_2 mixtures, natural gas and high purity hydrogen gas with the pressure of 0.4 MPa. Electron back scattered diffraction (EBSD) was employed to observe the fracture crack patterns in order to better understand the HE behaviour of X80 in the testing conditions. To elucidate the effect of CO_2 on hydrogen uptake, density functional theory (DFT) calculations were performed to characterize hydrogen-metal interactions in the CO_2-free and CO_2-containing systems.

2.0 EXPERIMENTAL AND COMPUTATIONAL DETAILS

2.1 Fatigue crack growth rate (FCGR) tests

X80 pipeline steel, which is commonly used for transmission pipelines, was used in this study. The ultimate tensile strength and 0.2% proof stress of the steel were 724 MPa and 660 MPa, respectively. The chemical composition (wt. %) is 0.06C-1.77Mn-0.21Si-0.26Cr-0.25Mo-0.006P-0.002S-0.02Ni-0.01Cu-bal.Fe. As shown in Fig. 1a, the average grain size of the steel was shown to be approximately 2.27 μm under EBSD.

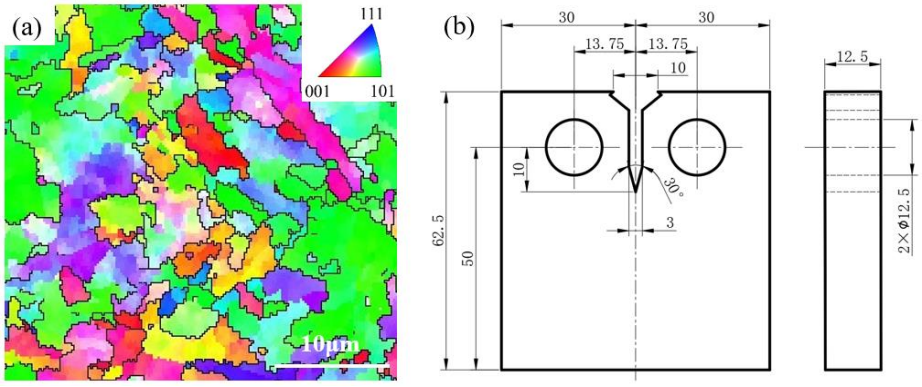

Figure 1. (a) EBSD maps of X80 pipeline steel, and (b) geometries of CT specimen

Compact-tension (CT) specimens with a width of 50 mm and a thickness of 12.5 mm, as shown in Fig. 1b, were used for FCGR tests. The specimens were sampled in the transverse-longitudinal orientation of the raw pipe. The surfaces of the specimens were mechanically polished with 2000 grid SiC papers and then cleaned ultrasonically in acetone. According to ASTM standard E647-15 [23], a pre-crack was first introduced from the starter notch in each specimen by applying cyclic loading at a frequency of 5 Hz and a stress ratio of 0.1. Subsequently, formal tests were performed under a constant load range to measure the FCGR (da/dN) versus stress intensity factor range (ΔK) at a test frequency of 1 Hz and a stress ratio of 0.1. Both pre-cracking and formal tests were conducted in the same environment at room temperature. In this study, an actual natural gas (NG) with a composition of $88.53CH_4$-$6.87C_2H_6$-$0.0014CO_2$-$2.41N_2$-other gases (units in molar mass%) was used. The purity of hydrogen and nitrogen gas used in the test was 99.9995%. FCGR tests were conducted in 0.4 MPa H_2, 0.4 MPa NG, 0.36 MPa NG+0.04 MPa H_2, 0.36 MPa N_2+0.04 MPa H_2, 0.35998 MPa N_2+0.04 MPa H_2 +0.02 kPa CO_2, 0.3598 MPa N_2+0.04 MPa H_2 +0.2 kPa CO_2, 0.358 MPa N_2+0.04 MPa H_2 +2 kPa CO_2. All tests were repeated three times. After loading, the fracture paths were observed by EBSD at an accelerating voltage of 15 kV.

2.2 Density functional theory calculations

To investigate the effect of CO_2 on the process of hydrogen entry into metallic materials at the atomic level, density functional theory (DFT) [24, 25] calculations were performed. The calculation in this work was completed in the Vienna Ab-initio Simulation Package (VASP) [26]. The electron-ion interactions were described by the projector-augmented wave (PAW) [27] method, and the electron exchange and correlation were modelled with Perdew–Burke–Ernzerhof (PBE) [28] method. The graphical visualization package VESTA [29] was used throughout this study. The object in this study is the α-Fe(110) plane, which has the lowest surface energy. The slab model was designed with 5 layers of Fe(110)-p(3×3) structure separated by a vacuum spacing of 12 Å to avoid the inter-slab interaction. The coordinates of the atoms in the bottom two layers were fixed, while the top three layers were fully relaxed. A Γ-centered *k*-point mesh of 3×3×1 was used for the slab model. Γ-centered *k*-point mesh of 9×9×9 for the bulk iron lattice and 1×1×1 for the free H_2 and CO_2.

It is known that the process of hydrogen entry into metals can be divided into the following four stages: adsorption, dissociation, dissolution and diffusion [30]. The adsorption, dissociation and dissolution stages have a general term, namely the surface interaction stage. To investigate the energetics of the above process, geometry optimization and climbing nudged elastic band (CI-NEB) [31] calculations were used in the calculations. The adsorption energy of gas A, E_{ads}, is given by

$$E_{ads} = E_{slab+A+B} - E_{slab} - E_A - E_B \quad (1)$$

where $E_{slab+A+B}$ – the total energy of the relaxed slab with gas A and B adsorbed, eV; E_{slab} – the total energy of the gas-free slab, eV; E_A – the energy of the free gas A, eV; E_B – the energy of the free gas B. All calculations converged to 10^{-6} eV/atom for the total energy and 0.03 eV/Å for the atomic force. A plane wave cut-off energy value of 400 eV and spin-polarization were performed.

3. RESULTS AND DISCUSSION

3.1 Fatigue crack growth rate

The relationships between d*a*/d*N* and Δ*K* of X80 pipeline steel measured under all test conditions are shown in Fig. 2. As reported in many materials previously, the results show that the FCGRs in the hydrogen-containing environments are faster than that in natural gas [11, 12]. The FCGRs measured in 0.36 MPa NG+0.04 MPa H_2 and 0.36 MPa N_2+0.04 MPa H_2 are all close to that in 0.4 MPa H_2, all of which are not much higher than that in natural gas. This indicates that X80 pipeline steel is not highly sensitive to the hydrogen-containing environment with a pressure of 0.4 MPa. For this material, the enhanced hydrogen embrittlement was not significant as found in our previous study of GB20# steel [19]. One of the reasons for this phenomenon may be the different microstructures and grain sizes of these two materials. GB20# steel consists of polygonal ferrite and lamellar pearlite and the average grain size is around 26 μm. For X80 pipeline steel, it comprises polygonal ferrite and granular bainite and the average grain size is much finer (2.27 μm) than that of GB20# steel. However, when the content of CO_2 in the hydrogen-containing mixture gradually increases from 0.005vol% to 0.5vol%, FCGR increases obviously and is faster than that in pure hydrogen gas when the content of CO_2 exceeds 0.05vol%. The FCGR in 0.358 MPa N_2+0.04 MPa H_2 +2 kPa CO_2 is about 1.52 times faster than that in 04 MPa H_2 at ΔK = 50 MPa·m$^{1/2}$. It is similar to the results of GB20# steel that the interaction between CO_2 and hydrogen has a deteriorating effect on the fatigue performance of steel and the degree increases with the increase of CO_2 content. Noting that the content of CO_2 in the natural gas used in this study was very low. This may be one of the reasons for the unobvious CO_2 effect on the FCGR of X80 pipeline steel in HENG.

3.2 Observations of the fatigue crack paths

Figure 3 shows the inverse pole figure (IPF) and kernel average misorientation (KAM) maps of the cracks formed in hydrogen and CO_2-containing hydrogen environments at ΔK = 50 MPa·m$^{1/2}$. The direction of crack propagation is from left to right, perpendicular to the loading direction. As shown in Fig. 3a and 3b, the crack in the hydrogen is a transgranular fracture, while the intergranular fracture (indicated by the white line) can be observed on the fracture path in 0.358 MPa N_2+0.04 MPa H_2+2 kPa CO_2. The small cracks generated at the grain boundaries expand and merge, and eventually form the main crack. As a result, the crack path in the CO_2-containing hydrogen environment is more tortuous and bifurcated. From the KAM image, it can be found that the plastic deformation in hydrogen is more server than that in the CO_2-containing hydrogen mixture. The plastic deformation

distribution area in hydrogen is larger than that in the CO_2-containing hydrogen environment as well. Depending on the material properties and loading conditions, the externally applied energy can be released either by crack growth (new surface cracks) or plastic deformation (e.g. dislocation movement, mechanical twinning or phase transition) or in most cases by a mixed mode of both [32]. In the present study, the relatively large plastic zone and the low FCGR suggest that the energy is mainly released by plastic deformation. Since no phase transition or mechanical twinning was observed on the fracture path, it can be inferred that the dislocation motion from the crack tip outward into the material matrix contributes significantly to the plastic energy release. Therefore, the crack path for the case of lower FCGR shows a larger plastic zone and smaller crack advancement.

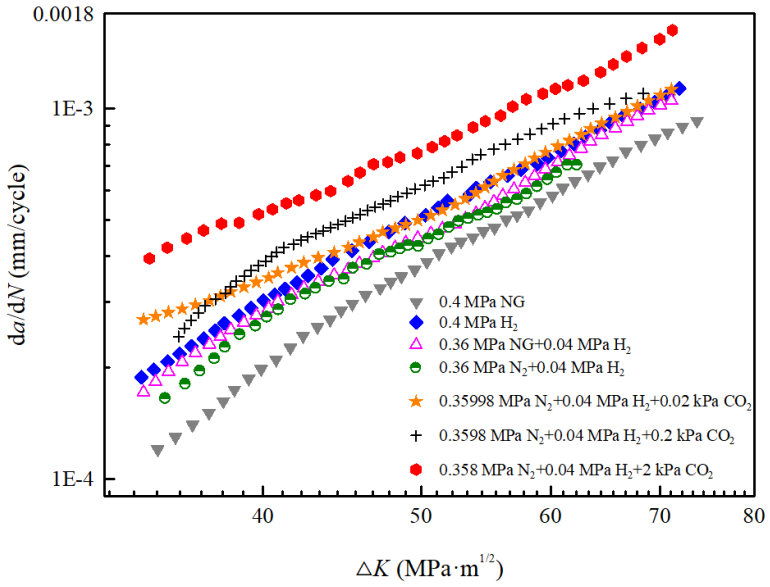

Figure 2. Relationships between da/dN and ΔK of X80 pipeline steel under different test conditions.

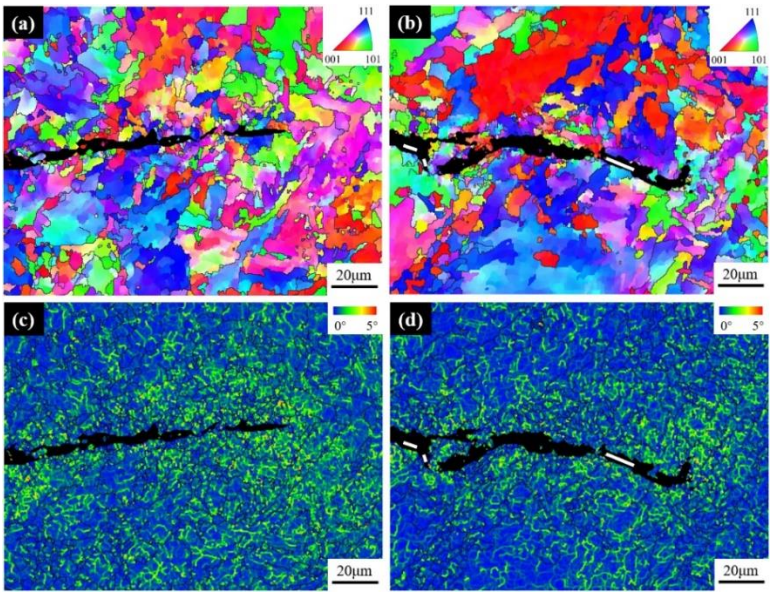

Figure 3. (a)(b) IPF and (c)(d) KAM micrographs of the crack paths formed in (a)(c) 0.4 MPa H_2 and (b)(d) 0.358 MPa N_2+0.04 MPa H_2+2 kPa CO_2 at ΔK = 50 MPa·m$^{1/2}$. The crack growth directions are from left to right.

The above macroscopic mechanical property and microscopic crack path characterization reveal that the enhanced HE of X80 may be mainly due to the promoted hydrogen uptake under the function of CO_2. This can result in a higher hydrogen concentration at grain boundaries. Moreover, cracks tend to develop around grain boundaries with high hydrogen concentration [33]. As a result, there is a change

in the fracture mode of steel from the complete transgranular fracture in hydrogen to a mixture of transgranular and intergranular fracture in the CO_2-containing mixture.

3.3 Hydrogen entry process at atom scale under CO_2 effect

Based on the above study, CO_2 has the potential to shorten the hydrogen-metal surface interaction time and thus improve hydrogen uptake in the metal. DFT calculations were chosen to investigate the mechanism of the CO_2 effect on the process of hydrogen entry into materials from an atomic perspective. The focus is on the adsorption, dissociation and dissolution of H_2 in the clean system as well as in the CO_2-containing system. The diffusion of H within the bulk is far away from the surface and it is difficult to be affected by the adsorbate on the surface.

3.3.1 Adsorption energetics of hydrogen on the Fe(110) surface

3.3.1.1 Adsorption behaviour of CO_2 on the Fe(110) surface

CO_2 is stable and is difficult to dissociate on the iron surface. During the FCGR experiments, CO_2 should always remain in a molecule state, moving freely or adsorbed on the surface. It is clear that CO_2 barely affects hydrogen uptake when it is far away from the iron surface. In this work, the energetics of the adsorption, dissociation and dissolution of H_2 on a CO_2 pre-adsorbed Fe(110) surface were investigated. We first calculate the geometric configuration and adsorption energy of CO_2 adsorbed on the Fe(110) surface. It is well known that there are four different potential adsorption sites for adsorbate on the Fe(110) surface: on-top of an iron atom from the top surface layer (T site), in between two Fe atoms either in a short or long-bridge position (SB and LB sites, respectively), or surrounded by three surface Fe atoms arranged in an isosceles triangle (H site) [34]. At the above adsorption sites, we established the initial model of CO_2 molecule adsorption on the iron surface. As shown in Fig. 4, the initial configurations of the twelve adsorption sites consist of four vertical sites and eight horizontal sites.

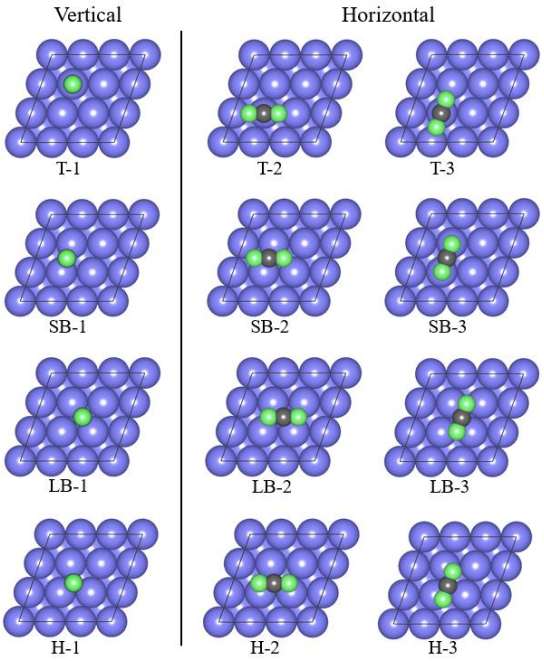

Figure 4. The twelve initial configurations of CO_2 adsorbed on the Fe(110) surface.

The results of the geometric optimization and adsorption energy of CO_2 adsorbed on various sites are given in Table 1. The adsorption energy of CO_2 on the Fe(110) surface ranges from -0.40 to 0.19 eV. The adsorption energy shows that molecular carbon dioxide tends to adsorb horizontally on the Fe(110) surface. The carbon dioxide molecule is found to have a strong adsorption energy on the H-3 sites with an adsorption energy of -0.40 eV, which is close to the value of -0.48 eV for CO_2 adsorption on similar structures calculated by Wang et al. [35]. The carbon-to-oxygen distance ($d_{C\text{-}O}$) is relaxed by 1.18 Å for the free gas to 1.30 Å and 1.29 Å with the smallest distance of 1.37 Å between C atom and the iron surface ($d_{C\text{-}slab}$), indicating that the iron surface has a strong attraction for CO_2 molecule.

The O-C-O bond angle ($\alpha_{c\text{-}o\text{-}c}$) also narrows from 180° for the free gas to 124°, indicating that a large number of electrons are generated near the C atom and the bond angle is changed by the repulsive effect of electrons.

Table 1. The adsorption energies of CO_2 at twelve sites on the Fe(110) surface and the configurations of CO_2 upon adsorption.

Initial adsorption sites		E_{ads}/eV	$d_{c\text{-}o}$/Å	$d_{c\text{-}slab}$/Å	$\alpha_{c\text{-}o\text{-}c}$/°
Vertical	T-1	0.00	1.18, 1.18	4.20	180
	SB-1	0.01	1.18, 1.18	4.31	180
	LB-1	0.00	1.18, 1.18	4.37	180
	H-1	-0.01	1.18, 1.18	4.35	180
Horizontal	T-2	0.19	1.28, 1.29	1.88	129
	T-3	0.19	1.28, 1.28	1.89	131
	SB-2	-0.12	1.28, 1.31	1.52	130
	SB-3	-0.26	1.25, 1.25	1.66	137
	LB-2	-0.39	1.30, 1.30	1.41	130
	LB-3	-0.39	1.30, 1.30	1.38	130
	H-2	-0.38	1.30, 1.29	1.42	130
	H-3	-0.40	1.30, 1.31	1.37	124

3.3.1.2 Coadsorption of CO_2 and H_2 on the Fe(110) surface

Based on the obtained most stable adsorption structure of CO_2 (see Fig. 5a), the initial configurations of Fe+H_2 and Fe+H_2+CO_2 systems were constructed. H_2 at different heights with full relaxation was optimized to get the most stable state of H_2 adsorbed on the Fe(110) surface in each system, and the calculated results are shown in Fig. 5b and 5c. The adsorption energy of H_2 on the clean Fe(110) surface is -0.46 eV, which is in good agreement with the previous results of -0.412 eV and -0.42 eV [35]. $d_{H\text{-}H}$ and $d_{H\text{-}slab}$ are 0.94 Å and 1.56 Å, respectively. When CO_2 is adsorbed on the surface, $d_{H\text{-}H}$ (0.95 Å) and $d_{H\text{-}slab}$ (1.56 Å) change less. However, the adsorption energy of H_2 decreases significantly, by 110.87% for the Fe+H_2+CO_2 system compared to the Fe+H_2 system. This means that the CO_2 adsorbed on the iron surface increases the adsorption ability of hydrogen on the surface. It is worth noting that the adsorption energy of CO_2 is close to that of H_2. It means that CO_2 can absorb on the iron surface as easily as H_2. However, H_2 adsorption on the surface is an exothermic process with no activation barrier and the adsorption of H_2 on the iron surface is found to be proceeding fast [35]. Therefore, the actual effect of CO_2 on the adsorption of hydrogen on the iron surface is small at the beginning of hydrogen and metal surface interaction.

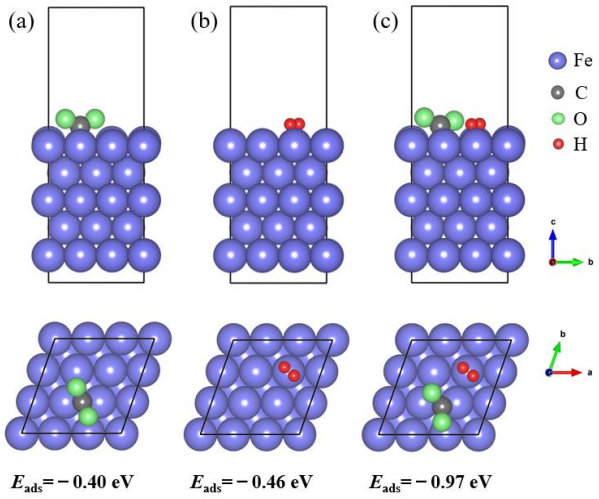

Figure 5. Stable adsorption configuration of (a) CO_2 and (b) H_2 on clean Fe(110) surface, and H_2 on CO_2-preadorbed Fe(110) surface.

3.3.2 Dissociation and dissolution energetics of hydrogen in different systems

Further investigation using the CI-NEB method was performed to study the energy barrier for hydrogen dissociation and dissolution under the CO_2 effect. Each transition state structure has been verified to have only one imaginary frequency.

The converged minimum energy paths (MEP) for the hydrogen dissociation in the CO_2-free and CO_2-containing systems obtained by CI-NEB calculation are shown in Fig. 6. The side view and top view of the dissociation path of H_2 on the clean surface and CO_2-preadsorbed surface are shown in Fig. 6 as well. The activation barriers and reaction energies of H_2 dissociation in the CO_2-free and CO_2-containing systems are summarized in Table 2. The results show that the dissociation barrier and dissociation energy of the hydrogen molecule on the CO_2-free surface is 0.02 eV and -1.37 eV, respectively, which are in general agreement with the previous calculations of 0.1 eV [36] and -1.39 eV [37]. When one CO_2 molecule is pre-adsorbed on the surface, the potential barriers and dissociation energy turn to be 0.01 eV and -1.26 eV, respectively. The similar dissociation barriers and dissociation energies for H_2 in the two systems suggest that CO_2 has little influence on the rate of H_2 dissociation on the iron surface. This is because H_2 has a high affinity and is easily dissociated when adsorbed on the pure Fe(110) surface [36]. Even though the surface site at a certain distance from H_2 is occupied by CO_2, H_2 still has the strong ability to dissociate.

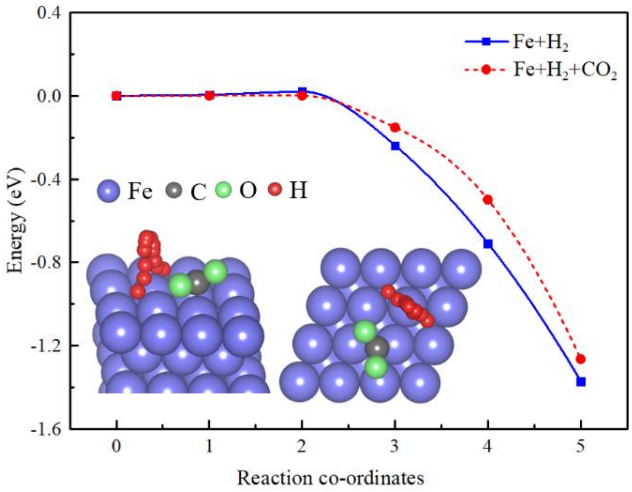

Figure 6. Minimum energy paths for the dissociation of H_2 on the clean and CO_2-preadsorbed Fe(110) surface.

The potential energy along the dissolution paths of the dissociated hydrogen atoms in the CO_2-free and CO_2-containing systems are shown in Fig. 7, as well as the top view and side view of the path in the Fe+H_2+CO_2 system. The dissociated two H atoms are first adsorbed on the surface hollow site, and then one of them passes through the small barrier between adjacent Fe atoms to reach the subsurface and finally dissolves between the surface and subsurface. As shown in Table 2, the energy in the process of hydrogen dissolution is positive, indicating that it is an endothermic process. Compared with the CO_2-free system, the atomic hydrogen dissolution barrier in the Fe+H_2+CO_2 system decreases to 0.77 eV and the dissolution energy decreases to 0.75 eV. The low barrier and reaction energy suggest that H is much easier to migrate from surface to subsurface when CO_2 is adsorbed on the iron surface. The decrease in dissolution energy increases the probability of atomic hydrogen entering the iron subsurface, while the decrease in dissolution activation energy greatly increases the rate of H dissolution. The rate constant k of H dissolution can be estimated using the Arrhenius relation in the following equation:

$$k = Ae^{-\frac{E_a}{RT}} \quad (2)$$

Where A – a preexponential factor, 1; R – the gas constant, J/(mol·K); T – the temperature, 298 K; E_a – the activation barrier taken from Table 2, eV. It can be calculated that the dissolution rate constant of H in the CO_2-free and CO_2-containing systems are 4.23×10^{-18} and 1.02×10^{-13}, respectively. The H

dissolution rate is accelerated by over 4 orders of magnitude under the CO_2 effect.

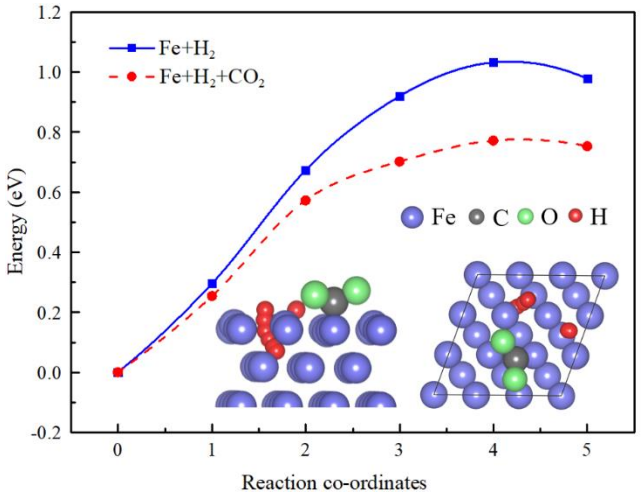

Figure 7. Minimum energy paths for the dissolution of H atom in the clean and CO_2-containing systems.

Table 2. Activation barriers and reaction energies for the H_2 dissociation and H dissolution in the different systems.

Systems	H_2 dissociation activation energy / eV	H_2 dissociation energy / eV	H_2 dissolution activation energy / eV	H_2 dissolution energy / eV
$Fe+H_2$	0.02	-1.37	1.03	0.98
$Fe+H_2+CO_2$	0.01	-1.26	0.77	0.75

To understand why the H atom dissolution is much easier in the CO_2-containing system than that in the CO_2-free system, we investigated the Bader population and electron densities for the surface Fe atoms in the CO_2-free and CO_2-containing systems. The average charge of the surface Fe atoms is +0.04 electron in the CO_2-free system. The charge of H on the CO_2-free surface is -0.35 electron for the surface hydrogen and -0.35 electron for the subsurface hydrogen. The negative charge suggests that on the surface and close to the surface hydrogen exists as hydride anion. For the CO_2-containing system, the charge of H is -0.33 for the surface hydrogen and -0.34 for the subsurface hydrogen. The average charge of the surface Fe atoms is +0.15 electron, which is more than that for the clean surface due to CO_2 adsorption. It can be concluded that the positive charge on the surface Fe atoms favours the hydride anion migration through the surface layer.

We compare planar slices through the electron densities of surface Fe atoms for slab without and with CO_2 adsorbed. As shown in Fig. 8, the surface layer is electron rich with significant interatomic electron density in the case of a clean slab. The high electron density between the surface Fe atom would be an effective barrier for hydrogen dissolution. However, for the slab with CO_2 adsorbed, the surface layer is electron poor with low interatomic electron density. The low electron density would significantly reduce the barrier for the migration of hydrogen atom from the surface to the subsurface.

3.4 Mechanism of hydrogen-assisted cracking under CO_2 effect

The results of the DFT calculations above show that CO_2 adsorbed on the iron surface strengthens H_2 adsorption and significantly increases the dissolution rate of dissociated H atoms dissolved to the material subsurface. Due to the fast adsorption rate of H_2 on the iron surface, the actual effect of CO_2 on hydrogen adsorption is small. The greatly reduced diffusion energy barrier of the dissociated hydrogen atoms from the surface to the subsurface by CO_2 is the major reason for the faster entry of hydrogen atoms into the metal in the CO_2/H_2 mixture. Although the computational model is simplified, the results can still qualitatively explain the enhanced HE of pipeline steel by CO_2 found in the FCGR experiments. In addition, gas-phase hydrogen permeation tests show that the hydrogen penetration time in the CO_2-blended mixture was shorter than in the pure hydrogen environment,

confirming the hydrogen uptake enhanced by CO_2 [13]. The fast dissolution of H into iron bulk will increase the content of dissolved H in iron bulk, enhancing the HE of pipeline steel.

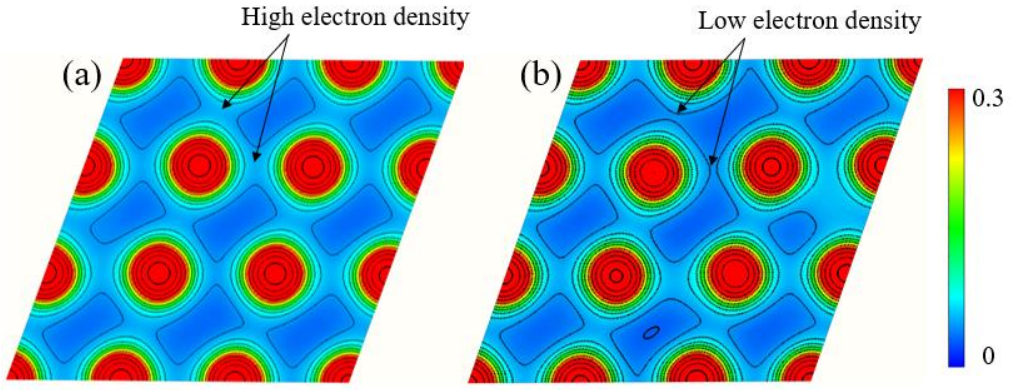

Figure 8. Plane slice through the electron densities of a surface Fe atom in the (a) clean and (b) CO_2-containing systems.

A schematic diagram of the fatigue crack propagation process in a pure hydrogen environment and an environment mixed with carbon dioxide is given in Fig. 9. It is appeared to establish a 'link' between results from both experiments and DFT calculations. In a pure hydrogen environment, hydrogen molecules undergo adsorption-dissociation-dissolution and then hydrogen atoms accumulate at the crack tip or diffuse within the metal bulk. However, when the material is exposed to a mixture of hydrogen and carbon dioxide, the dissociated hydrogen atoms accelerate to migrate from surface to subsurface when carbon dioxide is adsorbed on the iron surface. The fast dissolution of H into iron bulk can increase the content of dissolved H in iron bulk. Furthermore, the sites vacated by the dissolved hydrogen atoms re-supply adsorption and dissociation sites for the free gas-phase hydrogen molecules. Then, the newly dissociated hydrogen atoms are accelerated into the material by the influence of carbon dioxide again. As a result, the hydrogen concentration in the material tested in a hydrogen/carbon dioxide mixture is higher than that in hydrogen gas.

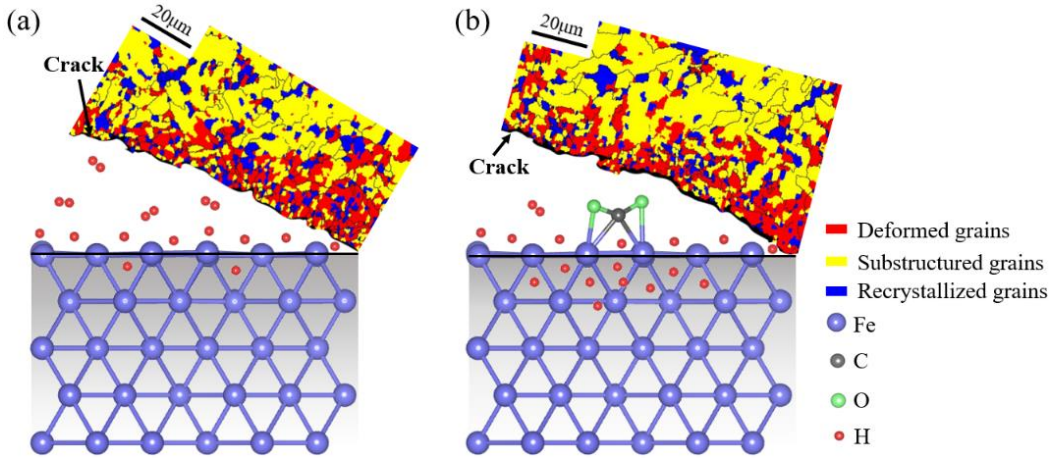

Figure 9. Schematic of crack propagation enhanced by CO_2 in a hydrogen-containing environment. Explanation in text. Upper right corners of (a) and (b) are DefRex plots of the crack paths in 0.4 MPa H_2 and 0.358 MPa N_2+0.04 MPa H_2+2 kPa CO_2 at ΔK = 50 MPa·m$^{1/2}$ for X80 pipeline steel, respectively.

Some researchers proposed that hydrogen may form pairs or clusters and even interact with interstitial carbon atoms to peg edge dislocations at a high hydrogen concentration, thereby slowing down the mobility of screw dislocations and decreasing their mobility [38]. In general, the dislocation pegging effect becomes more significant and the plastic deformation zone around the crack decreases when the hydrogen concentration around the crack tip grows higher [13]. This pinning effect embrittles the material and causes it to be more susceptible to hydrogen-assisted fracture at low stress. DefRex plots

of the crack paths in 0.4 MPa H_2 and 0.358 MPa N_2+0.04 MPa H_2+2 kPa CO_2 at ΔK = 50 MPa·$m^{1/2}$ for X80 steel are shown in the upper right corner of Fig. 9a and Fig. 9b, respectively, where deformed grains are shown in red, recrystallized grains in blue, and substructured grains in yellow. Consistent with the KAM plot results in Fig. 3, the densely distributed area of deformed grains around the crack in the CO_2-blended hydrogen environment is reduced compared to that in the pure hydrogen environment, reflecting the deterioration of the plastic deformability of X80 pipeline steel.

During the process of crack development, new surfaces are formed and the difference in hydrogen invasion under the CO_2 effect is always present on each new surface. Furthermore, it is difficult to reach an equilibrium between the hydrogen concentration in the lattices and in the trapping sites around the crack tip when the crack propagates rapidly. In this case, the time for hydrogen and metal surface interaction directly affects the final hydrogen concentration in the material. As we discussed before, CO_2 adsorbed on the metal surface can significantly shorten the time for hydrogen to migrate from the surface to the subsurface. Therefore, when the CO_2 is sufficient, the hydrogen content around the crack tip in the CO_2/H_2 mixtures will be higher than that in hydrogen during the whole process of crack growth. Under the influence of high hydrogen concentration, the dislocation mobility and the plastic deformation zone decrease, eventually leading to a faster crack growth rate and deterioration of mechanical properties in the CO_2-containing hydrogen environment.

4. CONCLUSIONS

In this study, FCGR experiments combined with DFT calculations were used to investigate the HE behaviour and mechanism of X80 pipeline steel under the effect of HENG as well as the mixtures of carbon dioxide and hydrogen. The main conclusions obtained from the current study are as follows:

(1) The FCGR in the HENG, which has less CO_2, is slower than that in the high purity hydrogen gas. However, when the content of CO_2 increases to 0.05vol%, the FCGR is higher than that in hydrogen. The FCGR enhancement by CO_2 further increases with the increase of CO_2 content.

(2) Observation of fracture crack paths by EBSD reveals that the fracture mode of steel changes from a transgranular fracture in hydrogen to a mixture of transgranular and intergranular fracture in the CO_2-containing mixture. Furthermore, the plasticity confines to the nearby areas close to the crack path in the presence of CO_2.

(3) DFT calculation results show that CO_2 can strengthen the adsorption of H_2 and fasten the dissolution (migration from surface to subsurface) of the H atom when CO_2 is adsorbed on the iron surface. Due to the fast adsorption of H_2 itself, the promoted H dissolution rate by CO_2 is the major reason for the enhanced hydrogen uptake and HE of the steel.

REFERENCES

1. Aprea, J.L., and Bolcich, J.C., The energy transition towards hydrogen utilization for green life and sustainable human development in Patagonia, *International Journal of Hydrogen Energy*, **45**, 2020, pp. 25627-25645.
2. Hermesmann, M., Grübel, K., Scherotzki, L., and Müller, T., Promising pathways: The geographic and energetic potential of power-to-x technologies based on regeneratively obtained hydrogen, *Renewable Sustainale Energy Review*, **138**, 2021, pp. 110644.
3. Messaoudani, Z.L., Rigas, F., Hamid, M.D.B., and Hassan, C.R.C., Hazards, safety and knowledge gaps on hydrogen transmission via natural gas grid: A critical review, *International Journal of Hydrogen Energy*, **41**, 2016, pp. 17511-17525.
4. Isaac, T., HyDeploy: The UK's First Hydrogen Blending Deployment Project, *Clean Energy*, **3**, 2019, pp. 114-125.
5. Messaoudani, Z.L., Rigas, F., Hamid, M.D.B., and Hassan, C.R.C., Hazards, safety and knowledge gaps on hydrogen transmission via natural gas grid: A critical review, *International Journal of Hydrogen Energy*, **41**, 2016, pp. 17511-17525.
6. Quarton, C.J., and Samsatli, S., Power-to-gas for injection into the gas grid: What can we learn from real-life projects, economic assessments and systems modelling?, *Renewable Sustainale Energy Review*, **98**, 2018, pp. 302-316.
7. Nelson, H.G., Hydrogen Embrittlement, (Briant, C.L., and Banerji S.K. Eds.), Elsevier, Netherlands, 1983, p. 275-359.
8. Oriani, R., Hydrogen embrittlement of steels, *Annual Review of Materials Science*, **8**, 1978, pp.

327-357.
9. Meng, B., Gu, C., Zhang, L., Zhou, C., Li, X., Zhao, Y., Zheng, J., Chen, X., and Han, Y., Hydrogen effects on X80 pipeline steel in high-pressure natural gas/hydrogen mixtures, *International Journal of Hydrogen Energy*, **42**, 2017, pp. 7404-7412.
10. Shang, J., Zheng, J., Hua, Z., Li, Y., Gu, C., Cui, T., and Meng, B., Effects of stress concentration on the mechanical properties of X70 in high-pressure hydrogen-containing gas mixtures, *International Journal of Hydrogen Energy*, **45**, 2020, pp. 28204-28215.
11. Nguyen, T.T., Park, J.S., Kim, W.S., Nahm, S.H., and Beak, U.B., Effect of low partial hydrogen in a mixture with methane on the mechanical properties of X70 pipeline steel, *International Journal of Hydrogen Energy*, **45**, 2020, pp. 2368-2381.
12. Nguyen, T.T., Park, J.S., Kim, W.S., Nahm, S.H., and Beak, U.B., Environment hydrogen embrittlement of pipeline steel X70 under various gas mixture conditions with in situ small punch tests, *Material Science and Engineering A*, **781**, 2020, pp. 139114.
13. Zhou, C., He, Y., Jiang, J., Zhang, K., Tang, D., Zhu, H., Shang, J., Sun, G., Wang, M., and Zhang, L., Hydrogen uptake induced by CO_2 enhances hydrogen embrittlement of iron in hydrogen blended natural gas, *Corrosion Science*, **207**, 2022, pp. 110594.
14. Frandsen, J.D., and Marcus, H.L., Environmentally assisted fatigue crack propagation in steel, *Metallurgical Transactions A*, **8**, 1977, pp. 265-272.
15. Barthélémy, H., Effects of pressure and purity on the hydrogen embrittlement of steels, *International Journal of Hydrogen Energy*, **36**, 2011, pp. 2750-2758.
16. Komoda, R., Kubota, M., Staykov, A., Ginet, P., Barbier, F., and Furtado, J., Inhibitory effect of oxygen on hydrogen-induced fracture of A333 pipe steel, *Fatigue Fracture Engineering Mechanics*, **42**, 2019, pp. 1387-1401.
17. Komoda, R., Yamada, K., Kubota, M., Ginet, P., Barbier, F., Furtado, J., and Prost, L., The inhibitory effect of carbon monoxide contained in hydrogen gas environment on hydrogen-accelerated fatigue crack growth and its loading frequency dependency, *International Journal of Hydrogen Energy*, **44**, 2019, pp. 29007-29016.
18. Xiong, M., Zheng, S., Qi, Y., Lv, Z., and Chen, Y., Effect of H_2/CO_2 partial pressure ratio on the tensile properties of X80 pipeline steel in the absence and presence of water, *International Journal of Hydrogen Energy*, **40**, 2015, pp. 11917-11924.
19. Shang, J., Chen, W., Zheng, J., Hua, Z., Zhang, L., Zhou, C., and Gu, C., Enhanced hydrogen embrittlement of low-carbon steel to natural gas/hydrogen mixtures, *Scripta Materialia*, **189**, 2020, pp. 67-71.
20. Shang, J., Wang, J., Chen, W., Wei, H., Zheng, J., Hua, Z., Zhang, L., and Gu, C., Different effects of pure hydrogen vs. hydrogen/natural gas mixture on fracture toughness degradation of two carbon steels, *Materials Letters*, **296**, 2021, pp. 129924.
21. Nelson, H., Hydrogen-induced slow crack growth of a plain carbon pipeline steel under conditions of cyclic loading, (Thompson, A. Ed.), Metallurgical Society of AIME, United States, 1976, p. 602-611.
22. Fukuyama, S., and Yokogawa, K., Prevention of hydrogen environmental assisted crack growth of 2. 25Cr-Mo steel by gaseous inhibitors, Verband der Technischen Uberwachungs-Vereine, Germany, 1992, pp. 914-923.
23. ASTM E647-15. Standard Test Method for Measurement of Fatigue Crack Growth Rates. 2015.
24. Hohenberg, P., and Kohn, W., Inhomogeneous Electron Gas, *Physicial Review*, **136**, 1964, pp. B864-B871.
25. Kohn, W., and Sham, L.J., Self-Consistent Equations Including Exchange and Correlation Effects, *Physicial Review*, **140**, 1965, pp. A1133-A1138.
26. Kresse, G., and Furthmüller, J., Efficient iterative schemes for ab initio total-energy calculations using a plane-wave basis set, *Physicial Review B*, **54**, 1996, pp. 11169-11186.
27. Blöchl, P.E., Projector augmented-wave method, *Physicial Review B*, **50**, 1994, pp. 17953-17979.
28. Perdew, J.P., Burke, K., and Ernzerhof, M., Generalized Gradient Approximation Made Simple, *Physical Review Letters*, **77**, 1996, pp. 3865-3868.
29. Momma, K., and Izumi, F., VESTA 3 for three-dimensional visualization of crystal, volumetric and morphology data, *Journal of Applied Crystallography*, **44**, 2011, pp. 1272-1276.
30. Counts, W., Wolverton, C., and Gibala, R., First-principles energetics of hydrogen traps in α-Fe: Point defects, *Acta Materialia*, **58**, 2010, pp. 4730-4741.
31. Henkelman, G., Uberuaga, B.P., and Jónsson, H., A climbing image nudged elastic band method for finding saddle points and minimum energy paths, *Journal of Chemical Physics*, **113**, 2000, pp.

9901-9904.
32. Wan, D., Deng, Y., Meling, J.I.H., Alvaro, A., and Barnoush, A., Hydrogen-enhanced fatigue crack growth in a single-edge notched tensile specimen under in-situ hydrogen charging inside an environmental scanning electron microscope, *Acta Materialia*, **170**, 2019, pp. 87-99.
33. Connolly, M., Martin, M., Bradley, P., Lauria, D., Slifka, A., Amaro, R., Looney, C., and Park, J.S., In situ high energy X-ray diffraction measurement of strain and dislocation density ahead of crack tips grown in hydrogen, *Acta Materialia*, **180**, 2019, pp. 272-286.
34. Cremaschi, P., Yang, H., and Whitten, J.L., Ab initio chemisorption studies of H on Fe (110), *Surface Science*, **330**, 1995, pp. 255-264.
35. Wang, H., Nie, X., Chen, Y., Guo, X., and Song, C., Facet effect on CO_2 adsorption, dissociation and hydrogenation over Fe catalysts: Insight from DFT, *Journal of CO_2 Utilization*, **26**, 2018, pp. 160-170.
36. Staykov A., Yamabe J., and Somerday B.P., Effect of hydrogen gas impurities on the hydrogen dissociation on iron surface, *International Journal of Quantum Information*, **114**, 2014, pp. 626-635.
37. Staykov, A., Komoda, R., Kubota, M., Ginet, P., Barbier, F., and Furtado, J., Coadsorption of CO and H_2 on an Iron Surface and Its Implication on the Hydrogen Embrittlement of Iron, *Journal of Physical Chemistry C*, **123**, 2019, pp. 30265-30273.
38. Caillard, D., A TEM in situ study of alloying effects in iron. II—Solid solution hardening caused by high concentrations of Si and Cr, *Acta Materialia*, **61**, 2013, pp. 2808-2827.